




Universal composite pulses for robust quantum state engineering in four-level systemsZhi-Cheng Shi ^{1,2}, Jian-Hui Wang,^{1,2} Cheng Zhang,^{1,2} Jie Song,³ and Yan Xia ^{1,2,*}¹*Fujian Key Laboratory of Quantum Information and Quantum Optics (Fuzhou University), Fuzhou 350108, China*²*Department of Physics, Fuzhou University, Fuzhou 350108, China*³*Department of Physics, Harbin Institute of Technology, Harbin 150001, China* (Received 11 September 2023; revised 9 January 2024; accepted 6 February 2024; published 29 February 2024)

We propose a protocol for robust quantum state engineering using composite pulses (CPs) in four-level systems. The analytical expression of the propagator is derived for the implementation of universal single-qubit gates and the maximum superposition state. By carefully designing the relative phases between pulses, the CP sequences can compensate for the pulse area error to any desired order. We present two classes of CP sequences, one generating robust population inversion and the other generating robust superposition states. As applications, we employ the well-designed CP sequences to achieve the conversion of the W and Greenberger-Horne-Zeilinger states with high fidelity in a Rydberg atomic system. It is shown that the CP sequences yield excellent robustness with respect to the pulse area errors, and they possess a short evolution time.

DOI: [10.1103/PhysRevA.109.022441](https://doi.org/10.1103/PhysRevA.109.022441)**I. INTRODUCTION**

Accurate and robust coherent control is one of the prerequisites for the development of quantum computation and quantum information [1]. Recent years have witnessed different techniques [2–6] to improve the precision of coherent control. Among them, adiabatic control is a traditional technique used for robustly implementing quantum state transitions, but the defects are also obvious, i.e., a low evolution rate and imperfect fidelity [7,8]. A promising candidate for overcoming these defects is the composite pulse technique, which combines the advantages of both the ultrahigh accuracy of resonant pulses and the robustness of adiabatic controls.

Composite pulses (CPs), originally developed in nuclear magnetic resonance (NMR) [9–12], are composed of multiple single pulses with distinct phases. By simply controlling the relative phases, CPs allow researchers to compensate for various systematic errors in the field of quantum computations [13,14]. Because of this unique advantage, CPs have been widely applied in different quantum systems, such as trapped ions [15–24], cold atoms [25–27], and quantum dots [28–30].

Heretofore, studies of CPs have mainly focused on the achievement of high-fidelity quantum gates [31–33], efficient detection of chiral molecules [34,35], robust preparation of quantum states [36–38], etc. In particular, recent confirmatory experiments were devoted to testing various CP sequences in an IBM quantum computer [39,40]. Remarkably, however, studies on CPs have been limited to two- and three-level systems, with little attention given to multilevel systems.

It is well known that qudits [41,42] with a multilevel structure are more favorable in quantum chemistry [43] and quantum simulation [44,45]. For instance, if there are N qudits that transform from a two-level structure to a four-

level one, the computational space will be extended from 2^N to 4^N [46–48]. This expansion can effectively save hardware resources without increasing the hardware complexity in quantum-computation platforms [41]. Moreover, a larger computational capacity and higher computational accuracy have also attracted considerable attention in multilevel systems [49].

Up to now, multiphoton adiabatic passage [50], tunable nonlinear optical amplification and attenuation [51], the quantum phase transition [52], frequency up-conversion amplification without inversion [53], and coherent transfer of optical vortices [54] have been successively implemented in four-level systems. More recently, there have been an increasing number of works [55,56] devoted to achieving population transfer in four-level systems. Despite the demonstrated potential of the four-level systems in various applications, most studies [50–56] hardly focus on investigating how to suppress the unknown errors in physical parameters. To take full advantage of the additional degrees of freedom of a four-level system, more control fields are always required, accompanied by an increase in the risk of operational errors [57]. Therefore, our goal is to develop the CP technique in four-level systems so that coherent control can still enable us to maintain high precision in an error-prone environment.

In this work, we achieve robust quantum state engineering by using composite pulses in four-level systems. The analytical formula for the propagator is first derived to prepare universal single-qubit gates and a maximum superposition state in this system. We then focus on realizing high-fidelity and robust coherent control via properly modulating the phases of CP sequences. It is shown that the errors in the pulse areas can be compensated to any desired order. Finally, the CP sequence is applied in Rydberg atomic systems, making it error-resilient in the conversion between the W and Greenberger-Horne-Zeilinger (GHZ) states at a short evolution time.

*xia-208@163.com

II. PHYSICAL MODEL AND GENERAL THEORY

A. General form of the propagator

The four-level system of interest has a ladder-type structure in which only adjacent energy-level transitions are allowed. This particular system can be embodied in the hyperfine levels of some alkali-metal atoms [58], and it enables us to observe some interesting phenomena, such as electromagnetically induced transparency [59–61]. In the interaction picture, the total Hamiltonian of this four-level system reads ($\hbar = 1$)

$$H = \Omega_1 e^{i\phi} |1\rangle\langle 2| + \Omega_2 e^{i\varphi} |2\rangle\langle 3| + \Omega_3 e^{i\Phi} |3\rangle\langle 4| + \text{H.c.}, \quad (1)$$

where the transitions $|m\rangle \leftrightarrow |m+1\rangle$ ($m = 1, 2, 3$) are driven by control fields with Rabi frequencies Ω_m , and the corresponding phases are ϕ , φ , and Φ . We assumed that the system works in the resonance condition for simplicity.

Note that the Hamiltonian (1) is widely studied in several physical systems, for instance the Rydberg atom used for realizing highly efficient Rydberg excitation by chirped multiphoton adiabatic passage [50] and the spin chain applied to achieve quantum information transmission at both ends [62,63]. More specifically, the Hamiltonian of a spin chain in the single-excitation subspace is actually equivalent to the Hamiltonian with a ladder-type structure [62,63]. In addition, such a Hamiltonian can also be adopted to characterize other four-level structures with similar dipole transitions in the double-ladder-type [64], N -type [59,65–67], and mirror-reflected N -type systems [68–71], where no more than two dipole transitions share a single level.

Assuming that all parameters in the Hamiltonian (1) are time-independent, the propagator of this system becomes $U = \exp(-iHT)$ at the evolution time T . After some calculations, the propagator can be written in a brief form,

$$U = \sum_{m=1}^4 \sum_{n=1}^4 U_{mn} |m\rangle\langle n|, \quad (2)$$

with

$$\begin{aligned} U_{11} &= \cos^2 \theta_1 \cos \theta_s + \sin^2 \theta_1 \cos \theta_c, \\ U_{22} &= \cos^2 \theta_2 \cos \theta_s + \sin^2 \theta_2 \cos \theta_c, \\ U_{33} &= \cos^2 \theta_1 \cos \theta_c + \sin^2 \theta_1 \cos \theta_s, \\ U_{44} &= \cos^2 \theta_2 \cos \theta_c + \sin^2 \theta_2 \cos \theta_s, \\ U_{13} &= U_{31}^* = \cos \theta_1 \sin \theta_1 (\cos \theta_c - \cos \theta_s) e^{i(\phi+\varphi)}, \\ U_{24} &= U_{42}^* = \sin \theta_2 \cos \theta_2 (\cos \theta_c - \cos \theta_s) e^{i(\varphi+\Phi)}, \\ U_{14} &= -U_{41}^* = i(\cos \theta_1 \sin \theta_2 \sin \theta_s - \sin \theta_1 \cos \theta_2 \sin \theta_c) e^{i\gamma}, \\ U_{23} &= -U_{32}^* = i(\sin \theta_1 \cos \theta_2 \sin \theta_s - \cos \theta_1 \sin \theta_2 \sin \theta_c) e^{i\varphi}, \\ U_{12} &= -U_{21}^* = -i(\cos \theta_1 \cos \theta_2 \sin \theta_s + \sin \theta_1 \sin \theta_2 \sin \theta_c) e^{i\phi}, \\ U_{34} &= -U_{43}^* = -i(\sin \theta_1 \sin \theta_2 \sin \theta_s + \cos \theta_1 \cos \theta_2 \sin \theta_c) e^{i\Phi}. \end{aligned}$$

In Eq. (2), we have set

$$\tan 2\theta_1 = \frac{2A_1 A_2}{A_3^2 + A_2^2 - A_1^2}, \quad (3a)$$

$$\tan 2\theta_2 = \frac{2A_2 A_3}{A_3^2 - A_2^2 - A_1^2}, \quad (3b)$$

$$\theta_s = A_1 \sec \theta_1 \cos \theta_2, \quad (3c)$$

$$\theta_c = A_1 \csc \theta_1 \sin \theta_2, \quad (3d)$$

$$\gamma = \phi + \varphi + \Phi, \quad (3e)$$

where $A_m = \Omega_m T$ ($m = 1, 2, 3$) represents the pulse area of the m th control field. The detailed derivation of the propagator (2) can be found in Appendix A.

Despite a slight difference in form, the propagator (2) we derive here is actually equivalent to the one in Ref. [72], where the Lie algebra based on dynamical symmetry is utilized to construct the expressions for three Rabi frequencies. Under a proper transformation of physical parameters, these two expressions can be converted to each other. For details, one can refer to Appendix B.

B. Single-qubit gates

In this subsection, we demonstrate that universal single-qubit gates can be obtained in this four-level system, where the states $|1\rangle$ and $|4\rangle$ are encoded as a qubit. The general form of a single-qubit gate in the basis $\{|1\rangle, |4\rangle\}$ can be written as

$$U(\alpha, \beta) = \begin{bmatrix} \cos \alpha & ie^{i\beta} \sin \alpha \\ ie^{-i\beta} \sin \alpha & \cos \alpha \end{bmatrix}, \quad (4)$$

where α and β are determined by the desired quantum gate. It is worth mentioning that Eq. (4) is not just a single-qubit gate, it may have other uses in specific physical systems. For example, through setting $\alpha = \pi/4$, we can obtain a GHZ state in the Rydberg atomic system (see also the details in Sec. IV), when three atoms are initially at the ground state $|0\rangle$ [72–74]. Besides, we can realize quantum state transfer between two ends of a chain with four spins if α is equal to $\pi/2$ [62,63].

To achieve this single-qubit gate, only focusing on the elements U_{11} and U_{41} in Eq. (2) is insufficient, and we must ensure that there is no population leakage to the states $|2\rangle$ and $|3\rangle$. Starting from the general expressions for Eqs. (2) and (4), the elements U_{m1} ($m = 1, 2, 3$) have to satisfy the following relations:

$$U_{11} = \cos \alpha, \quad U_{21} = U_{31} = 0, \quad (5)$$

where the element U_{41} can be directly derived by the normalization condition. Note that the constraints in Eq. (5) automatically lead to $U_{42} = U_{43} = 0$, because $U_{21} = -U_{43}$ and $\cos \theta_c - \cos \theta_s = 0$. Moreover, the phase β in Eq. (4) is exactly equal to the phase γ given by Eq. (3e). After some calculations, the analytical solutions for Eq. (5) read

$$A_1 = A_3 = \sqrt{\alpha(2k\pi - \alpha)}, \quad (6a)$$

$$A_2 = 2(k\pi - \alpha), \quad (6b)$$

where k is a positive integer and $0 < \alpha < 2k\pi$; see Appendix C for details.

C. Maximum superposition state

Another quantum operation performed in this four-level system is to achieve population transfer from the state $|2\rangle$ to the maximum superposition state $(|1\rangle + |4\rangle)/\sqrt{2}$. The reason for preparing this superposition state is that it can be used for the conversion between the W and GHZ states [75–79]. To

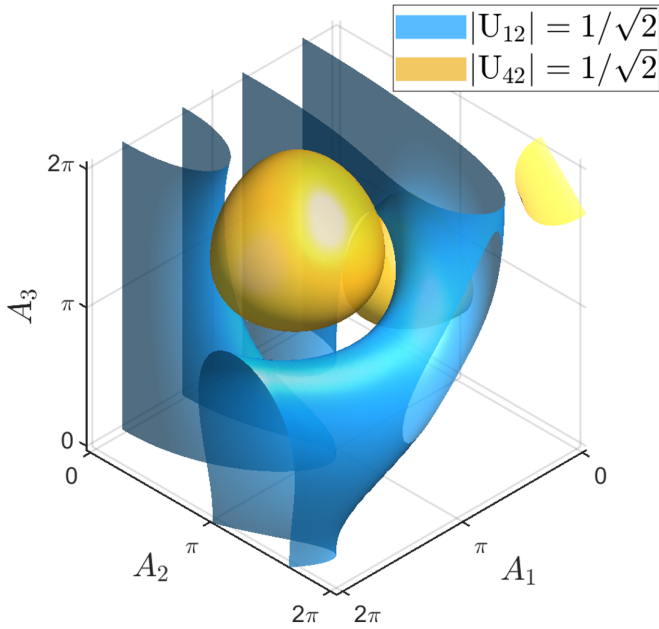


FIG. 1. Two-dimensional surfaces for Eq. (7).

this end, we must set $|U_{12}| = |U_{42}| = 1/\sqrt{2}$ in the propagator (2). Namely, the equations to be solved become

$$\cos\theta_1 \cos\theta_2 \sin\theta_s + \sin\theta_1 \sin\theta_2 \sin\theta_c = \frac{1}{\sqrt{2}}, \quad (7a)$$

$$\sin\theta_2 \cos\theta_2 (\cos\theta_c - \cos\theta_s) = \frac{1}{\sqrt{2}}, \quad (7b)$$

where we also consider the probability amplitude in the target state, and the relative phase between the states $|1\rangle$ and $|4\rangle$ can be properly modulated by ϕ , φ , and Φ .

Due to the complexity, it is difficult to directly derive an analytical form of the solutions for Eq. (7), and we turn to find numerical solutions instead. According to Eqs. (3a)–(3d), three pulse areas A_m ($m = 1, 2, 3$) can be regarded as unknowns of Eq. (7). To obtain feasible solutions for three pulse areas, we respectively plot two-dimensional surfaces of these two subequations in the three-dimensional space. Then, the intersectant curves or points of two surfaces are actually the solutions to Eq. (7). Through this method, we are able to find all possible solutions for three pulse areas. In Fig. 1, we show the two-dimensional surfaces of Eq. (7) within a certain range of three pulse areas. Obviously, these points at which two surfaces intersect are the feasible solutions to three pulse areas, and one group of them are

$$A_1 = 1.225, \quad A_2 = 1.420, \quad A_3 = 2.352. \quad (8)$$

Note that this numerical method is quite intuitive and can quickly find multiple solutions for the pulse areas A_m ($m = 1, 2, 3$). To achieve this goal, we extend the range of pulse areas in the three-dimensional space to display more points of intersection between two surfaces. Table I presents some other solutions for three pulse areas.

TABLE I. Other solutions of the pulse areas for the realization of the superposition state $(|1\rangle + |4\rangle)/\sqrt{2}$ driven from the initial state $|2\rangle$.

Index	A_1	A_2	A_3
1	4.560	1.542	5.055
2	2.558	3.389	5.433
3	1.277	5.318	7.628
4	6.224	4.017	8.427
5	5.020	6.260	10.177
6	2.564	7.137	10.413

III. ERROR COMPENSATION BY COMPOSITE PULSES

A. CPs for complete population inversion

We first study how to design CPs to implement accurate population inversion from the state $|1\rangle$ to $|4\rangle$. To this end, we can simply set $\alpha = \pi/2$ in Eq. (6), and the values of three pulse areas are ($k = 1$)

$$A_1 = A_3 = \frac{\sqrt{3}}{2}\pi, \quad A_2 = \pi. \quad (9)$$

Obviously, this is the simplest way to achieve complete population inversion. Nevertheless, this single pulse (Hamiltonian) is highly sensitive to errors, leading to the decline of the fidelity of population inversion.

To see it more clearly, suppose that there are errors in the pulse areas

$$A_m = A_m(1 + \epsilon_m), \quad (10)$$

with dimensionless parameter ϵ_m being the error magnitude of the m th pulse area, $m = 1, 2, 3$. Here, the errors ϵ_m are supposed to be unrelated to each other, and thus regarded as independent unknown variables. Through performing a Taylor expansion at $\epsilon_m = 0$, the transition probability of the target state $|4\rangle$ becomes

$$P_{41, \epsilon_{123}} = 1 - \left(\frac{3}{4} + \frac{9}{64}\pi^2 \right) (\epsilon_1^2 + \epsilon_3^2) - \frac{3\pi^2}{16} \epsilon_2^2 + \left(\frac{3}{2} - \frac{9\pi^2}{32} \right) \epsilon_1 \epsilon_3 + \dots \quad (11)$$

We can find from Eq. (11) that it is only accurate up to the second-order in the errors ϵ_m . In Figs. 2(a)–2(c), we plot the transition probability $P_{41, \epsilon_{123}}$ versus pulse area errors ϵ_m for the single pulse (Hamiltonian). The results show a rapid decrease in the transition probability near $\epsilon_m = 0$, directly proving that it is impossible to achieve robust population inversion with a single pulse (Hamiltonian).

To tackle this issue, we can employ CP sequences, which consist of multiple single pulses (Hamiltonians) with the same pulse area but different phases to be designated. For the sake of brevity, we use the label Θ_n to represent all phases in the n th pulse (Hamiltonian), i.e., $\Theta_n = \{\phi_n, \varphi_n, \Phi_n\}$. Then, the total propagator for an N -pulse sequence is achieved by the product of the propagator of each pulse (Hamiltonian),

$$U_{\epsilon_{123}}^N = U(\Theta_N)U(\Theta_{N-1}) \cdots U(\Theta_2)U(\Theta_1). \quad (12)$$

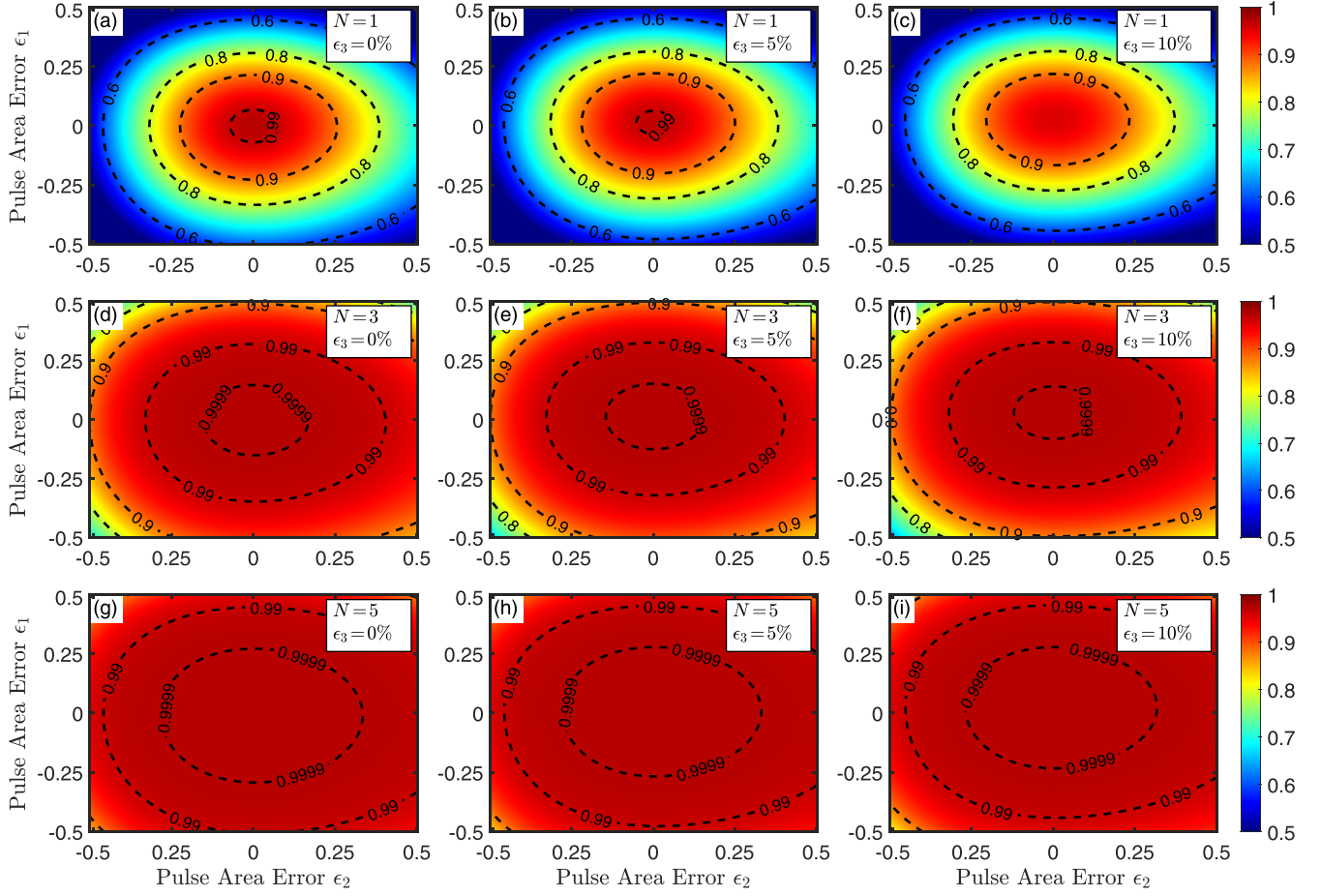


FIG. 2. Transition probability of the target state $|4\rangle$ vs pulse area errors for (a)–(c) the single pulse, (d)–(f) the three-pulse sequence, and (g)–(i) the five-pulse sequence. The pulse areas A_m satisfy Eq. (9) and all phases are given by the analytical solutions. One can see in panels (a)–(c) that the region of high transition probability ($P > 99.99\%$) hardly appears in the single pulse.

The transition probability $P_{41, \epsilon_{123}}^N$ of the target state $|4\rangle$ is determined by the element $U_{41, \epsilon_{123}}^N$ in the total propagator (12). Similar to the case of the single pulse (Hamiltonian), we divide the transition probability $P_{41, \epsilon_{123}}^N = |U_{41, \epsilon_{123}}^N|^2$ into multiple error terms by the Taylor expansion at $\epsilon_1 = \epsilon_2 = \epsilon_3 = 0$,

$$P_{41, \epsilon_{123}}^N = P_{41}^N + \sum_{j=0}^{\infty} \sum_{k=0}^{\infty} \sum_{l=0}^{\infty} s_{jkl} \epsilon_1^j \epsilon_2^k \epsilon_3^l, \quad (k + j + l \neq 0), \quad (13)$$

where P_{41}^N is the accurate transition probability of the target state $|4\rangle$ in the absence of errors, and s_{jkl} denote error coefficients greatly affecting the preselected transition probability. Note that the expressions for s_{jkl} are associated with not only Rabi frequencies, but also phases. Based on this feature, we can utilize the phases to reduce the impact of pulse area errors. To be specific, we design suitable Θ_n to nullify as many low-order error coefficients as possible while keeping the transition probability equal to 1 at $\epsilon_1 = \epsilon_2 = \epsilon_3 = 0$. That is,

$$P_{41}^N = \left| U_{41, \epsilon_{123}}^N \right|_{\epsilon_1 = \epsilon_2 = \epsilon_3 = 0}^2 = 1, \quad (14a)$$

$$s_{jkl} = \frac{1}{j!k!l!} \frac{\partial^{j+k+l}}{\partial \epsilon_1^j \partial \epsilon_2^k \partial \epsilon_3^l} \left| U_{41, \epsilon_{123}}^N \right|_{\epsilon_1 = \epsilon_2 = \epsilon_3 = 0}^2 = 0, \quad (14b)$$

where $j, k, l = 0, 1, 2, \dots$ and $j + k + l \neq 0$. When low-order error coefficients vanish, a relatively large plateau of high transition probability can appear in the vicinity of $\epsilon_1 = \epsilon_2 = \epsilon_3 = 0$, thereby attaining robust population inversion.

We next take specific pulse numbers to illustrate the design of the phases of CP sequence. According to Eq. (12), the total propagator of the three-pulse sequence reads

$$U_{\epsilon_{123}}^3 = U(\Theta_3)U(\Theta_2)U(\Theta_1). \quad (15)$$

Since the phases of the first pulse (Hamiltonian) do not affect the final transition probability, we simply set it to zero, i.e., $\phi_1 = \varphi_1 = \Phi_1 = 0$. It is worth stressing that the error coefficients s_{100} , s_{010} , and s_{001} in Eq. (14b) automatically vanish, because they contain the term $\sin k\pi$ or $\cos 3\alpha$. Furthermore, taking account of the symmetrical structure of Ω_1 and Ω_3 in propagator (2), we have $s_{jkl} = s_{lkj}$. Therefore, we can use six controllable phases $\{\phi_2, \varphi_2, \Phi_2, \phi_3, \varphi_3, \Phi_3\}$ to solve the following equations:

$$s_{110} = s_{101} = s_{200} = s_{020} = s_{111} = s_{210} = 0, \quad (16)$$

where the numerical solutions are listed in Table II. It is worth mentioning that nullifying different third-order error coefficients leads to different robust performances, and we just select $s_{111} = s_{210} = 0$ here. According to these numerical solutions, we can infer its analytical form as

TABLE II. Phases of the three- and five-pulse sequences for population inversion and the maximum superposition state. The subscript ϵ_{123} in the sequence $U_{\epsilon_{123}}^N$ ($S_{\epsilon_{123}}^N$) represents the compensation for three pulse area errors, while the subscript ϵ_m in $U_{\epsilon_m}^N$ indicates the compensation for the corresponding error ϵ_m .

Sequence	Three pulses						Five pulses											
	ϕ_2	φ_2	Φ_2	ϕ_3	φ_3	Φ_3	ϕ_2	φ_2	Φ_2	ϕ_3	φ_3	Φ_3	ϕ_4	φ_4	Φ_4	ϕ_5	φ_5	Φ_5
$U_{\epsilon_{123}}^N$	3.144	3.140	2.095	1.050	6.280	5.239	3.120	3.172	1.237	5.627	0.063	4.348	2.498	3.186	1.847	1.252	6.275	5.037
$S_{\epsilon_{123}}^N$	3.587	5.281	1.604	3.587	5.281	4.745	2.388	3.141	3.896	3.723	1.806	0.754	1.165	4.948	4.359	1.165	4.948	1.218
$U_{\epsilon_1}^N$	3.142	3.142	4.189	5.236	6.283	1.047	3.047	3.247	1.201	5.566	0.129	4.296	2.483	3.206	1.817	1.216	0.027	5.032
$U_{\epsilon_2}^N$	1.780	2.409	4.189	3.874	0.189	2.221	3.326	3.066	4.963	0.762	0.033	1.746	3.750	3.261	4.299	5.086	6.175	1.333
$U_{\epsilon_3}^N$	3.142	3.142	2.094	1.047	0.000	5.236	3.277	3.054	1.231	5.850	6.119	4.440	2.628	3.028	1.944	1.277	0.004	4.983

$\{\pi, \pi, 2\pi/3, \pi/3, 0, 5\pi/3\}$, which is verified to be the exact solutions for Eq. (16). After substituting the analytical solutions back into the transition probability, we find that $P_{41, \epsilon_{123}}^3$ is accurate to sixth order.

In Figs. 2(d)–2(f), we plot the transition probability $P_{41, \epsilon_{123}}^3$ of the target state $|4\rangle$ as a function of the first two pulse area errors ϵ_1 and ϵ_2 for the three-pulse sequence, where the third pulse area error ϵ_3 is set to 0%, 5%, and 10%, respectively. It is easily found that the three-pulse sequence provides a very broad area of high transition probability ($P > 99.99\%$), whereas the single pulse fails to reach this threshold. Remarkably, even if the error in the third pulse area increases to 10%, the system still maintains a high transition probability across a wide region.

The total propagator of the five-pulse sequence can be expressed as

$$U_{\epsilon_{123}}^5 = U(\Theta_5)U(\Theta_4)U(\Theta_3)U(\Theta_2)U(\Theta_1). \quad (17)$$

We now have 12 controllable phases that can be used for solving the equations

$$s_{110} = s_{101} = s_{200} = s_{020} = s_{111} = s_{210} = 0, \quad (18a)$$

$$s_{201} = s_{120} = s_{211} = s_{121} = s_{220} = s_{202} = 0, \quad (18b)$$

where the corresponding numerical solutions are presented in Table II.

Similar to the case of the three-pulse sequence, we can confirm that the analytical solutions for Eq. (18) are $\{\pi, \pi, 2\pi/5, 9\pi/5, 0, 7\pi/5, 4\pi/5, \pi, 3\pi/5, 2\pi/5, 0, 8\pi/5\}$, and $P_{41, \epsilon_{123}}^5$ is now accurate to the tenth order.

Figures 2(g)–2(i) show the transition probability $P_{41, \epsilon_{123}}^5$ of the state $|4\rangle$ as a function of the first two pulse area errors ϵ_1 and ϵ_2 for the five-pulse sequence, where the third pulse area error ϵ_3 is set to 0%, 5%, and 10%, respectively. We can see that the robustness against the pulse area errors ϵ_m can be further promoted by the five-pulse sequence. Such a result substantiates the effectiveness of our designed sequences for robust population inversion. Furthermore, it is easily observed that the robustness of the target state $|4\rangle$ against the pulse area errors becomes better as the number of pulses increases.

Next, we consider some special situations in which the three pulse areas have a certain correlation, such as $\epsilon_1 = \epsilon_2 = \epsilon_3 = \epsilon$. On this occasion, we can also utilize the Taylor expansion to construct CP sequences for compensation of the errors. Due to the reduction of the number of error terms,

it is easier to eliminate higher-order error coefficients under the same number of pulses. For details, one can refer to Appendix D.

B. CPs for the maximum superposition state

In this section, we construct another type of CP sequences, which produce the high-fidelity maximum superposition state in a robust manner. To achieve this goal, the equations to be satisfied become

$$P_{12}^N = P_{42}^N = \frac{1}{2}, \quad (19a)$$

$$a_{jkl} = \frac{1}{j!k!l!} \frac{\partial^{j+k+l}}{\partial \epsilon_1^j \partial \epsilon_2^k \partial \epsilon_3^l} |U_{12, \epsilon_{123}}^N|^2 \Big|_{\epsilon_1 = \epsilon_2 = \epsilon_3 = 0} = 0, \quad (19b)$$

$$b_{npq} = \frac{1}{n!p!q!} \frac{\partial^{n+p+q}}{\partial \epsilon_1^n \partial \epsilon_2^p \partial \epsilon_3^q} |U_{42, \epsilon_{123}}^N|^2 \Big|_{\epsilon_1 = \epsilon_2 = \epsilon_3 = 0} = 0, \quad (19c)$$

where Eq. (19a) indicates that the population of the states $|1\rangle$ and $|4\rangle$ maintains 1/2 in the absence of pulse area errors, and a_{jkl} and b_{npq} are the error coefficients of the transition probability from the state $|2\rangle$ to $|1\rangle$ and $|4\rangle$, respectively, $j, k, l, n, p, q = 0, 1, 2, \dots$. We numerically solve the phases for the three- and five-pulse sequences (labeled as the $S_{\epsilon_{123}}^3$ and $S_{\epsilon_{123}}^5$ sequences), and the corresponding solutions are given in Table II. For simplicity, we plot in Fig. 3 the fidelity of the superposition state $(|1\rangle + |4\rangle)/\sqrt{2}$ as a function of the first two pulse area errors ϵ_1 and ϵ_2 for the five-pulse sequence, where the third pulse area error ϵ_3 is set to 5%. Compared to the single pulse, the five-pulse sequence, as anticipated, provides a wider area of high fidelity.

IV. APPLICATIONS

The CP sequences we have derived above can be applied to realize the conversion between the W and GHZ states in a robust fashion. Recently, Zheng *et al.* achieved this conversion in the Rydberg atomic system by using the Lewis-Riesenfeld invariant (LRI) method [73]. Subsequently, a Lie-algebraic approach based on dynamical symmetries [72] was proposed to further reduce the evolution time. To be specific, at the same maximum amplitude of Rabi frequencies, the evolution time is about three times faster than that of the LRI method [73]. Afterwards, a quantum-brachistochrone formalism [80] was developed to obtain the time-optimal dynamical evolution

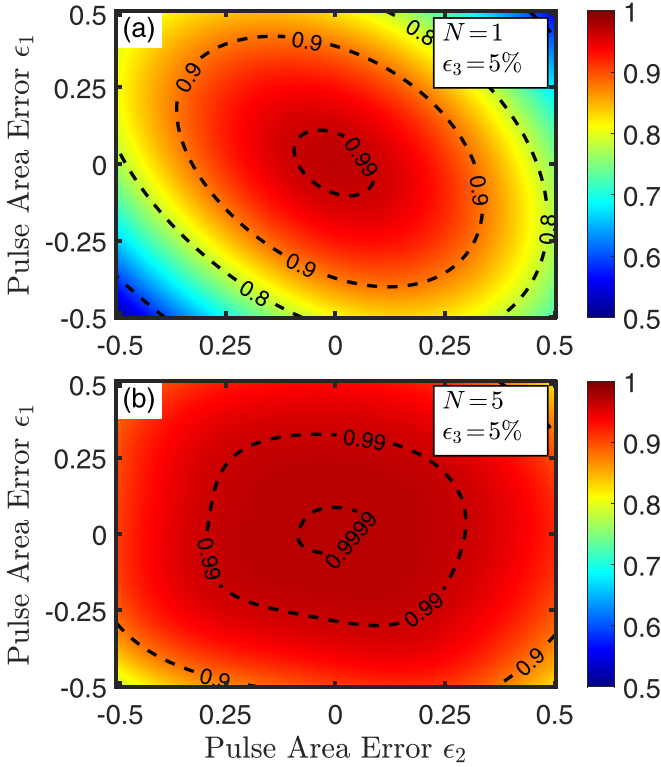


FIG. 3. Fidelity of the superposition state $(|1\rangle + |4\rangle)/\sqrt{2}$ vs pulse area errors for (a) the single pulse and (b) the five-pulse sequence. The fidelity is defined by $F = 1/2|(\langle 4| + \langle 2|)|\psi(T)\rangle|^2$. The pulse areas A_m satisfy Eq. (9) and the phases are given in Table II.

in this conversion [74], shorter than the above two methods [72,73].

It is imperative to point out that the existing methods [72–74] lack a specialized compensation for parameter errors, especially a deviation in driving fields. In the following, we employ the CP sequences for achieving this conversion in a robust way.

The physical system of interest involves three identical neutral atoms. As shown in Fig. 4(a), each atom has a ground state $|0_k\rangle$ and a Rydberg state $|r_k\rangle$, where the subscript k represents the k th atom, $k = 1, 2, 3$. All atoms are simultaneously driven by four driving fields with Rabi frequencies λ_m and the corresponding phases χ_m , $m = 1, 2, 3, 4$. Here, the fourth

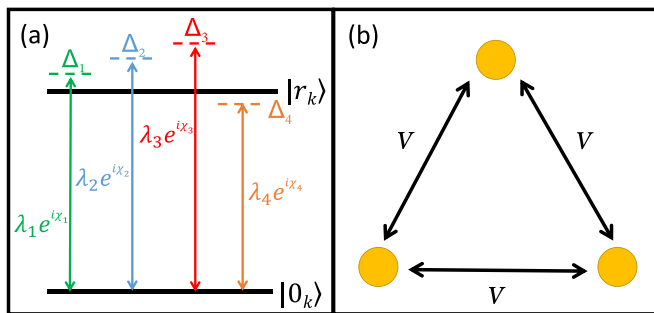


FIG. 4. (a) Energy-level structure of three identical Rydberg atoms driven by four external driving fields. (b) Rydberg interaction between adjacent atoms with strength V .

driving field is only employed to eliminate energy-level shifts [73]. Moreover, there is a detuning in each driving field and atom, labeled as Δ_m . As shown in Fig. 4(b), adjacent atoms have Rydberg interaction with strength V . Therefore, in the interaction picture, the system Hamiltonian reads

$$H(t) = \sum_{k=1}^3 \sum_{m=1}^4 [\lambda_m e^{i\chi_m} |0_k\rangle \langle r_k| + \Delta_m |r_k\rangle \langle r_k| + \text{H.c.}] + \sum_{p<q} V |r_p r_q\rangle \langle r_p r_q|, \quad (20)$$

where $p, q = 1, 2, 3$.

When the physical parameters satisfy

$$\{V, \Delta_4\} \gg \{\lambda_4, \Delta_1, \delta_2, \delta_3\} \gg \{\lambda_1, \lambda_2, \lambda_3\} \quad (21)$$

with $\delta_2 = V - \Delta_2$ and $\delta_3 = 2V - \Delta_3$, according to the second-order perturbation theory, we can ignore high-frequency components in Eq. (20), and the effective Hamiltonian of this system becomes [73]

$$H_{\text{eff}} = \sqrt{3}\lambda_1 e^{i(\chi_1 + (\Delta_1 + \xi_1)t)} |0_1 0_2 0_3\rangle \langle W| + \sqrt{3}\lambda_3 e^{i(\chi_3 + (\delta_3 + \xi_2)t)} |W'\rangle \langle r_1 r_2 r_3| + \lambda_2 \{e^{i(\chi_2 + (\delta_2 + \xi_3)t)} + 2e^{i(\chi_2 + (\delta_2 + \xi_4)t)}\} |W\rangle \langle W'| - \lambda_2 e^{i(\chi_2 + (\delta_2 + \xi_3)t)} (|0_1 0_2 r_3\rangle \langle r_1 r_2 0_3| + |0_1 r_2 0_3\rangle \langle r_1 0_2 r_3| + |r_1 0_2 0_3\rangle \langle 0_1 r_2 r_3|) + \text{H.c.}, \quad (22)$$

where

$$|W\rangle = \frac{1}{\sqrt{3}} (|0_1 0_2 r_3\rangle + |0_1 r_2 0_3\rangle + |r_1 0_2 0_3\rangle), \quad (23a)$$

$$|W'\rangle = \frac{1}{\sqrt{3}} (|r_1 r_2 0_3\rangle + |r_1 0_2 r_3\rangle + |0_1 r_2 r_3\rangle), \quad (23b)$$

$$\xi_1 = \frac{4\lambda_4^2}{\Delta_4 + V} - \frac{6\lambda_4^2}{\Delta_4}, \quad (23c)$$

$$\xi_2 = \frac{4\lambda_4^2}{\Delta_4 + V} - \frac{6\lambda_4^2}{\Delta_4 + 2V}, \quad (23d)$$

$$\xi_3 = -\frac{2\lambda_4^2}{\Delta_4 + V}, \quad (23e)$$

$$\xi_4 = \frac{3\lambda_4^2}{\Delta_4} - \frac{8\lambda_4^2}{\Delta_4 + V} + \frac{3\lambda_4^2}{\Delta_4 + 2V}. \quad (23f)$$

Once we set $\Delta_1 = -\xi_1$, $\delta_2 = -\xi_4$, $\delta_3 = -\xi_2$, and make the system satisfy the large detuning condition: $\delta_2 \gg \lambda_2$, the effective Hamiltonian (22) can be further simplified as

$$H'_{\text{eff}} = \Omega_1 e^{i\phi} |0_1 0_2 0_3\rangle \langle W| + \Omega_2 e^{i\varphi} |W\rangle \langle W'| + \Omega_3 e^{i\Phi} |W'\rangle \langle r_1 r_2 r_3| + \text{H.c.} \quad (24)$$

with $\Omega_1 = \sqrt{3}\lambda_1$, $\Omega_2 = 2\lambda_2$, $\Omega_3 = \sqrt{3}\lambda_3$, $\phi = \chi_1$, $\varphi = \chi_2$, and $\Phi = \chi_3$. It is easily found that the effective Hamiltonian (24) possesses a four-level structure studied in Sec. II A. Therefore, the conversion between the W and GHZ states can be viewed as population transfer between the states $|2\rangle$ and $(|1\rangle + |4\rangle)/\sqrt{2}$ in the four-level system, where $|\text{GHZ}\rangle = (|0_1 0_2 0_3\rangle + |r_1 r_2 r_3\rangle)/\sqrt{2}$.

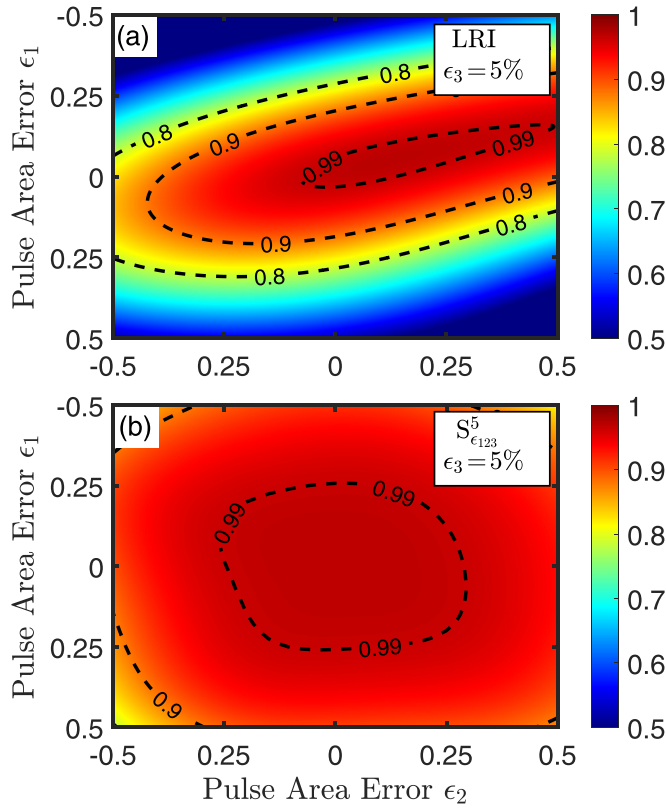


FIG. 5. GHZ-state fidelity vs pulse area errors for (a) the LRI method and (b) the $S_{\epsilon_{123}}^5$ sequence. The third pulse area error ϵ_3 is set to 5%.

Next, we investigate the robustness with respect to the pulse area errors by using CP sequences. In reality, due to the nonuniform spatial distribution of driving fields, neutral atoms may not be accurately manipulated. Besides, the intensity of driving fields varies over time, and thus always changes throughout the entire evolution process. These adverse factors may lead to errors in the pulse areas, which are denoted as $A'_m = A'_m(1 + \epsilon_m)$, where $A'_m = \lambda_m T$, $m = 1, 2, 3$. In this situation, we apply the $S_{\epsilon_{123}}^5$ sequence with the pulse areas given by Eq. (8) and the phases presented in Table II to realize the robust conversion between the W and GHZ states. To make a comparison between the $S_{\epsilon_{123}}^5$ sequence and the LRI method [73], we plot the GHZ-state fidelity $F = |\langle \text{GHZ} | \psi(T) \rangle|^2$ as a function of the pulse area errors in Fig. 5. The result shows that while the LRI method is somewhat robust to the error ϵ_2 in the second pulse area, the overall fidelity is not particularly high in the presence of pulse area errors. Especially, the center region of high fidelity is far away from $\epsilon_m = 0$, compromising the robustness for this system. In contrast, Fig. 5(b) shows that the $S_{\epsilon_{123}}^5$ sequence maintains high fidelity in the center region, regardless of how the errors in three pulse areas vary within a certain range. Obviously, the $S_{\epsilon_{123}}^5$ sequence may be a more suitable choice in an error-prone environment.

To see the robust performance more clearly, we now consider a special case of all errors being the same, i.e., $\epsilon_1 = \epsilon_2 = \epsilon_3 = \epsilon$. Such a case may occur when there is a deviation in the evolution time. Since there is only a single error ϵ , the solutions for the phases are different from those of the $S_{\epsilon_{123}}^N$

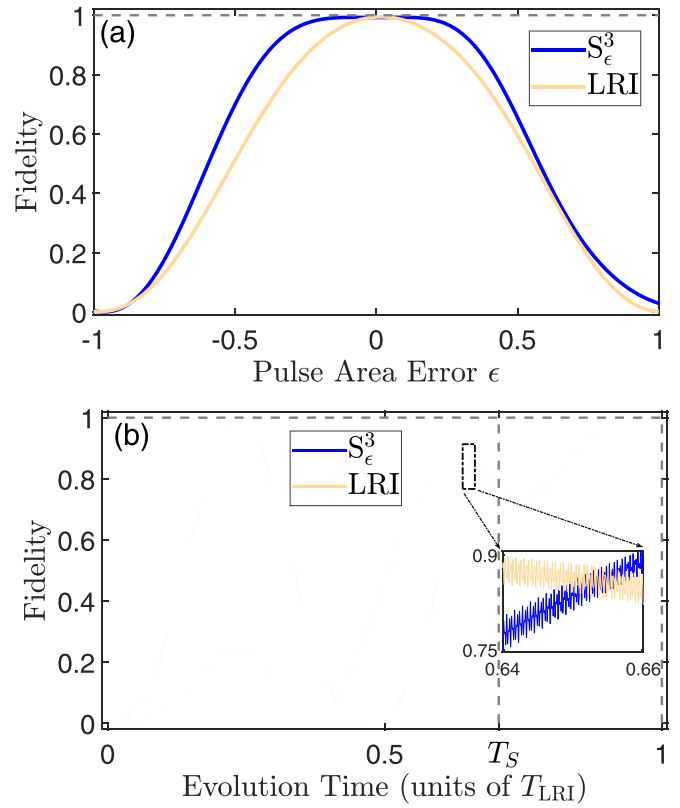


FIG. 6. (a) GHZ-state fidelity vs the pulse area error ϵ for the S_{ϵ}^3 sequence and the LRI method. (b) Time evolution of the GHZ-state fidelity using the S_{ϵ}^3 sequence and the LRI method. Note that the appearance of slight oscillations [e.g., see the inset in panel (b)] during the evolution process is due to the high-frequency components in the Hamiltonian (20).

sequence. For example, the phases of the three-pulse sequence (labeled as the S_{ϵ}^3 sequence) are

$$\Theta_2 = \{\phi_2, \varphi_2, \Phi_2\} = \{4.189, 3.142, 2.094\}, \quad (25a)$$

$$\Theta_3 = \{\phi_3, \varphi_3, \Phi_3\} = \{0.000, 1.047, 0.254\}. \quad (25b)$$

We plot the GHZ-state fidelity versus the error ϵ in Fig. 6(a). In the LRI method, it is necessary to demand high accuracy of Rabi frequencies and the evolution time to guarantee the validity of the conversion process. Once the system exhibits the pulse area errors, the GHZ-state fidelity significantly drops, as shown by the light solid curve in Fig. 6(a). For the S_{ϵ}^3 sequence, the fidelity profile is much flatter around $\epsilon = 0$, indicating greater robustness to the pulse area errors within a certain range.

Another important point that is worthy of attention is the evolution time. The time evolution of the GHZ-state fidelity is plotted in Fig. 6(b), where we employ the full Hamiltonian (20) rather than the effective Hamiltonian (24) to solve the Schrödinger equation. The total evolution time of the LRI method and the S_{ϵ}^3 sequence are denoted as T_{LRI} and T_S , respectively. We can see that, under the same maximum amplitude of Rabi frequencies, the evolution time is sharply reduced in the S_{ϵ}^3 sequence. Therefore, compared to the LRI method, the S_{ϵ}^3 sequence can achieve better robustness against the pulse area errors and possess a shorter evolution time.

V. CONCLUSION

In summary, we have implemented robust quantum state engineering by constructing CP sequences in four-level systems. Through deriving the analytical expression of the propagator, universal single-qubit gates are easily attained by properly choosing the pulse areas. Furthermore, we also prepare a maximum superposition state by numerically solving the pulse areas in a three-dimensional parameter space. To make the preparation process robust against pulse area errors, we take advantage of CP sequences in which the relative phases are designed for nullifying low-order error coefficients in the transition probability. We mainly construct two classes of CP sequences: one for robust population inversion and the other for robust preparation of the maximum superposition state. It is verified that both sequences work well even when the system exhibits various errors.

For applications, the well-designed CP sequences can be used for achieving the robust conversion of the W and GHZ states with high-fidelity in the Rydberg atomic system. The results demonstrate that the CP sequence can dramatically reduce the influence of pulse area errors in this conversion. Therefore, both advantages of robustness against errors and short evolution time are favorable for its experimental realization in an error-prone environment. We believe that the universality and flexibility of the proposed CP sequences make it a fascinating tool to implement high-fidelity quantum computations in multilevel systems.

ACKNOWLEDGMENTS

This work is supported by the Natural Science Foundation of Fujian Province under Grant No. 2021J01575, the Natural Science Funds for Distinguished Young Scholar of Fujian Province under Grant No. 2020J06011, and the Project from Fuzhou University under Grant No. JG202001-2.

APPENDIX A: DETAILED DERIVATION OF EQ. (2)

In this Appendix, we deduce in detail the analytical expression of the propagator without pulse area errors in the four-level system.

We first rewrite the system Hamiltonian (1) by means of eigenvalues and eigenstates, i.e.,

$$H = \sum_{i=1}^4 \lambda_i |E_i\rangle \langle E_i|, \quad (\text{A1})$$

with eigenvalues λ_i ,

$$\lambda_1 = -\lambda_2 = -\frac{1}{\sqrt{2}} \sqrt{\Omega_1^2 + \Omega_2^2 + \Omega_3^2 - \Omega'}, \quad (\text{A2})$$

$$\lambda_3 = -\lambda_4 = -\frac{1}{\sqrt{2}} \sqrt{\Omega_1^2 + \Omega_2^2 + \Omega_3^2 + \Omega'}, \quad (\text{A3})$$

and eigenstates $|E_i\rangle$,

$$|E_1\rangle = \frac{1}{\mathcal{N}} \left(\frac{\sqrt{\Omega_1^2 + \Omega_2^2 + \Omega_3^2 - \Omega'} (-\Omega_1^2 + \Omega_2^2 + \Omega_3^2 + \Omega')}{2\sqrt{2}\Omega_1} e^{i(\phi+\varphi+\Phi)}, \right. \\ \left. \frac{\Omega_1^2 + \Omega_2^2 - \Omega_3^2 - \Omega'}{2} e^{i(\varphi+\Phi)}, \frac{-\Omega_2 \sqrt{\Omega_1^2 + \Omega_2^2 + \Omega_3^2 - \Omega'}}{\sqrt{2}} e^{i\Phi}, \Omega_2 \Omega_3 \right)^\tau, \quad (\text{A4})$$

$$|E_2\rangle = \frac{1}{\mathcal{N}} \left(\frac{-\sqrt{\Omega_1^2 + \Omega_2^2 + \Omega_3^2 - \Omega'} (-\Omega_1^2 + \Omega_2^2 + \Omega_3^2 + \Omega')}{2\sqrt{2}\Omega_1} e^{i(\phi+\varphi+\Phi)}, \right. \\ \left. \frac{\Omega_1^2 + \Omega_2^2 - \Omega_3^2 - \Omega'}{2} e^{i(\varphi+\Phi)}, \frac{\Omega_2 \sqrt{\Omega_1^2 + \Omega_2^2 + \Omega_3^2 - \Omega'}}{\sqrt{2}} e^{i\Phi}, \Omega_2 \Omega_3 \right)^\tau, \quad (\text{A5})$$

$$|E_3\rangle = \frac{1}{\mathcal{N}} \left(\frac{\sqrt{\Omega_1^2 + \Omega_2^2 + \Omega_3^2 + \Omega'} (-\Omega_1^2 + \Omega_2^2 + \Omega_3^2 - \Omega')}{2\sqrt{2}\Omega_1} e^{i(\phi+\varphi+\Phi)}, \right. \\ \left. \frac{\Omega_1^2 + \Omega_2^2 - \Omega_3^2 + \Omega'}{2} e^{i(\varphi+\Phi)}, \frac{-\Omega_2 \sqrt{\Omega_1^2 + \Omega_2^2 + \Omega_3^2 + \Omega'}}{\sqrt{2}} e^{i\Phi}, \Omega_2 \Omega_3 \right)^\tau, \quad (\text{A6})$$

$$|E_4\rangle = \frac{1}{\mathcal{N}} \left(\frac{-\sqrt{\Omega_1^2 + \Omega_2^2 + \Omega_3^2 + \Omega'} (-\Omega_1^2 + \Omega_2^2 + \Omega_3^2 - \Omega')}{2\sqrt{2}\Omega_1} e^{i(\phi+\varphi+\Phi)}, \right. \\ \left. \frac{\Omega_1^2 + \Omega_2^2 - \Omega_3^2 + \Omega'}{2} e^{i(\varphi+\Phi)}, \frac{\Omega_2 \sqrt{\Omega_1^2 + \Omega_2^2 + \Omega_3^2 + \Omega'}}{\sqrt{2}} e^{i\Phi}, \Omega_2 \Omega_3 \right)^\tau, \quad (\text{A7})$$

where \mathcal{T} denotes transposition, the normalization coefficient \mathcal{N} reads $\mathcal{N} = \sqrt{(\Omega_1^2 + \Omega_2^2 - \Omega_3^2)^2 + (\Omega_1^2 + \Omega_2^2 - \Omega_3^2)\Omega'}$, and $\Omega' = \sqrt{(\Omega_1^2 + \Omega_2^2 - \Omega_3^2)^2 + 4\Omega_2^2\Omega_3^2}$.

Then, the form of the propagator at the evolution time T is given by

$$U = \sum_{i=1}^4 \exp(-i\lambda_i T) |E_i\rangle \langle E_i| = \sum_{m=1}^4 \sum_{n=1}^4 U_{mn} |m\rangle \langle n|, \quad (\text{A8})$$

with

$$\begin{aligned} U_{11} &= \frac{1}{2A_4} [(A_2^2 + A_3^2 - A_1^2 + A_4) \cos \theta_s + (-A_2^2 - A_3^2 + A_1^2 + A_4) \cos \theta_c], \\ U_{22} &= \frac{1}{2A_4} [(-A_2^2 + A_3^2 - A_1^2 + A_4) \cos \theta_s + (A_2^2 - A_3^2 + A_1^2 + A_4) \cos \theta_c], \\ U_{33} &= \frac{1}{2A_4} [(-A_2^2 - A_3^2 + A_1^2 + A_4) \cos \theta_s + (A_2^2 + A_3^2 - A_1^2 + A_4) \cos \theta_c], \\ U_{44} &= \frac{1}{2A_4} [(A_2^2 - A_3^2 + A_1^2 + A_4) \cos \theta_s + (-A_2^2 + A_3^2 - A_1^2 + A_4) \cos \theta_c], \\ U_{13} &= U_{31}^* = \frac{A_1 A_2}{A_4} (-\cos \theta_s + \cos \theta_c) e^{i(\phi+\varphi)}, \\ U_{24} &= U_{42}^* = \frac{A_2 A_3}{A_4} (-\cos \theta_s + \cos \theta_c) e^{i(\varphi+\Phi)}, \\ U_{14} &= U_{41}^* = \frac{-i\sqrt{2}}{A_4} \left(\frac{A_1 A_2 A_3}{\sqrt{A_1^2 + A_2^2 + A_3^2 - A_4}} \sin \theta_s - \frac{A_1 A_2 A_3}{\sqrt{A_1^2 + A_2^2 + A_3^2 + A_4}} \sin \theta_c \right) e^{i\gamma}, \\ U_{23} &= -U_{32}^* = \frac{iA_2}{\sqrt{2}A_4} \left(\sqrt{A_1^2 + A_2^2 + A_3^2 - A_4} \sin \theta_s - \sqrt{A_1^2 + A_2^2 + A_3^2 + A_4} \sin \theta_c \right) e^{i\varphi}, \\ U_{12} &= -U_{21}^* = \frac{-iA_1}{\sqrt{2}A_4} \left(\frac{-A_1^2 - A_2^2 + A_3^2 - A_4}{\sqrt{A_1^2 + A_2^2 + A_3^2 - A_4}} \sin \theta_s + \frac{A_1^2 + A_2^2 - A_3^2 + A_4}{\sqrt{A_1^2 + A_2^2 + A_3^2 + A_4}} \sin \theta_c \right) e^{i\phi}, \\ U_{34} &= -U_{43}^* = \frac{-iA_3}{\sqrt{2}A_4} \left(\frac{A_1^2 + A_2^2 - A_3^2 + A_4}{\sqrt{A_1^2 + A_2^2 + A_3^2 - A_4}} \sin \theta_s + \frac{-A_1^2 + A_2^2 - A_3^2 + A_4}{\sqrt{A_1^2 + A_2^2 + A_3^2 + A_4}} \sin \theta_c \right) e^{i\Phi}, \end{aligned}$$

where $A_m = \Omega_m T$, $m = 1, 2, 3$, $\gamma = \phi + \varphi + \Phi$, $A_4 = \sqrt{(A_1^2 + A_2^2 - A_3^2)^2 + 4A_2^2 A_3^2}$, and

$$\theta_s = \frac{\sqrt{A_2^2 + A_3^2 + A_1^2 - A_4}}{\sqrt{2}}, \quad (\text{A9a})$$

$$\theta_c = \frac{\sqrt{A_2^2 + A_3^2 + A_1^2 + A_4}}{\sqrt{2}}. \quad (\text{A9b})$$

Note that the element U_{11} can be rewritten as

$$\begin{aligned} U_{11} &= \frac{1}{2} \left(\frac{A_2^2 + A_3^2 - A_1^2}{A_4} + 1 \right) \cos \theta_s + \frac{1}{2} \left(\frac{A_1^2 - A_2^2 - A_3^2}{A_4} + 1 \right) \cos \theta_c, \\ &= \frac{1}{2} \left(\sqrt{\frac{1}{1 + \left(\frac{2A_1 A_2}{A_3^2 + A_2^2 - A_1^2} \right)^2}} + 1 \right) \cos \theta_s + \frac{1}{2} \left(1 - \sqrt{\frac{1}{1 + \left(\frac{2A_1 A_2}{A_3^2 + A_2^2 - A_1^2} \right)^2}} \right) \cos \theta_c. \end{aligned} \quad (\text{A10})$$

Through setting

$$\tan 2\theta_1 = \frac{2A_1 A_2}{A_3^2 + A_2^2 - A_1^2}, \quad (\text{A11})$$

the element U_{11} is reduced to

$$U_{11} = \cos^2 \theta_1 \cos \theta_s + \sin^2 \theta_1 \cos \theta_c. \quad (\text{A12})$$

In a similar way, the element U_{22} can be simplified as

$$U_{22} = \cos^2 \theta_2 \cos \theta_s + \sin^2 \theta_2 \cos \theta_c, \quad (\text{A13})$$

where

$$\tan 2\theta_2 = \frac{2A_2A_3}{A_3^2 - A_2^2 - A_1^2}. \quad (\text{A14})$$

Substituting Eqs. (A11) and (A14) into Eqs. (A9a) and (A9b), we can obtain the simplified expressions for θ_s and θ_c ,

$$\theta_s = A_1 \sec \theta_1 \cos \theta_2, \quad (\text{A15a})$$

$$\theta_c = A_1 \csc \theta_1 \sin \theta_2. \quad (\text{A15b})$$

APPENDIX B: EQUIVALENCY OF TWO PROPAGATORS

In this Appendix, we prove that the propagator given by Eq. (2) is equivalent to the one in Ref. [72].

First, we redefine four new variables that relate to Eq. (3) as follows:

$$\phi_\alpha = \frac{\pi}{2} - (\theta_1 + \theta_2), \quad (\text{B1a})$$

$$\phi_\beta = -\frac{\pi}{2} - (\theta_1 - \theta_2), \quad (\text{B1b})$$

$$\theta_\beta = \frac{1}{2}(\theta_c + \theta_s), \quad (\text{B1c})$$

$$\theta_\alpha = \frac{1}{2}(\theta_c - \theta_s). \quad (\text{B1d})$$

After substituting Eqs. (B1) into (2), the propagator can be expressed in terms of four new variables,

$$U' = \sum_{m=1}^4 \sum_{n=1}^4 U'_{mn} |m\rangle \langle n|, \quad (\text{B2})$$

with

$$U'_{11} = -\cos \theta_\alpha \cos \theta_\beta - \cos(\phi_\alpha + \phi_\beta) \sin \theta_\alpha \sin \theta_\beta,$$

$$U'_{22} = \cos \theta_\alpha \cos \theta_\beta - \cos(\phi_\alpha - \phi_\beta) \sin \theta_\alpha \sin \theta_\beta,$$

$$U'_{33} = -\cos \theta_\alpha \cos \theta_\beta + \cos(\phi_\alpha + \phi_\beta) \sin \theta_\alpha \sin \theta_\beta,$$

$$U'_{44} = \cos \theta_\alpha \cos \theta_\beta + \cos(\phi_\alpha - \phi_\beta) \sin \theta_\alpha \sin \theta_\beta,$$

$$U'_{13} = U'_{31} = -\sin \theta_\alpha \sin \theta_\beta \sin(\phi_\alpha + \phi_\beta),$$

$$U'_{24} = U'_{42} = \sin \theta_\alpha \sin \theta_\beta \sin(\phi_\alpha - \phi_\beta),$$

$$U'_{14} = U'_{41} = i(\sin \theta_\alpha \cos \theta_\beta \cos \phi_\alpha - \cos \theta_\alpha \sin \theta_\beta \cos \phi_\beta),$$

$$U'_{23} = U'_{32} = i(\sin \theta_\alpha \cos \theta_\beta \cos \phi_\alpha + \cos \theta_\alpha \sin \theta_\beta \cos \phi_\beta),$$

$$U'_{12} = U'_{21} = i(\sin \theta_\alpha \sin \theta_\beta \cos \phi_\alpha + \cos \theta_\alpha \sin \theta_\beta \sin \phi_\beta),$$

$$U'_{34} = U'_{43} = i(\sin \theta_\alpha \sin \theta_\beta \cos \phi_\alpha - \cos \theta_\alpha \sin \theta_\beta \sin \phi_\beta).$$

It is easy to find that Eq. (B2) is actually the expression for the propagator given in Ref. [72], when the system Hamiltonian is time-independent. Note that the phases are not considered in Ref. [72], and the expressions for three Rabi frequencies are derived via the dynamical-symmetry method

rather than Eq. (3). Although the derivation ways are different, these two propagators are equivalent to each other and connected by Eq. (B1).

APPENDIX C: DETAILED DERIVATION OF IMPLEMENTING SINGLE-QUBIT GATES

In this Appendix, we provide the detailed derivation of three pulse areas used to implement universal single-qubit gates, whose information is encoded in the states $|1\rangle$ and $|4\rangle$.

First, we solve the equation $U_{31} = 0$, i.e.,

$$\cos \theta_1 \sin \theta_2 (\cos \theta_s - \cos \theta_c) = 0. \quad (\text{C1})$$

Apparently, the solutions for Eq. (C1) are

$$\theta_1 = \pi/2 + k\pi, \quad \theta_2 = k\pi, \quad \theta_s = \pm\theta_c + 2k\pi, \quad (\text{C2})$$

where k is an arbitrary integer. Through substituting $\theta_1 = \pi/2 + k\pi$ into Eq. (3b), we find that either Ω_1 or Ω_2 vanishes. As a result, the four-level system degrades into a two- or three-level one, which is beyond our scope. A similar situation also occurs in the case of $\theta_2 = k\pi$. Therefore, these two solutions are discarded here. For the solution of $\theta_s = \pm\theta_c + 2k\pi$, we divide it in two cases,

$$\theta_c = \alpha, \quad \theta_s = -\alpha + 2k\pi, \quad (\text{C3a})$$

$$\theta_c = \alpha, \quad \theta_s = \alpha + 2k\pi, \quad (\text{C3b})$$

where α is an arbitrary real number.

For the first case (C3a), according to Eqs. (3c) and (3d), its specific form can be expressed as

$$A_1 \csc \theta_1 \cos \theta_2 = \alpha, \quad (\text{C4a})$$

$$A_1 \sec \theta_1 \cos \theta_2 = -\alpha + 2k\pi. \quad (\text{C4b})$$

After some calculations, the parameters θ_1 and θ_2 can be solved analytically,

$$\theta_1 = \pm \tan^{-1} \frac{\sqrt{(\alpha - 2k\pi)^2 - A_1^2}}{\sqrt{A_1^2 - \alpha^2}}, \quad (\text{C5a})$$

$$\theta_2 = \pm \tan^{-1} \frac{\alpha \sqrt{(\alpha - 2k\pi)^2 - A_1^2}}{(2k\pi - \alpha) \sqrt{A_1^2 - \alpha^2}}. \quad (\text{C5b})$$

Since the element U_{42} in the propagator also involves the term $(\cos \theta_s - \cos \theta_c)$, we have $U_{42} = 0$. At the same time, the elements U_{21} and U_{43} are reduced to

$$U_{21} = -U_{43} = i \frac{(2k\pi\alpha - \alpha^2 - A_1^2) \sin \alpha}{2(k\pi - \alpha)\Omega_1}. \quad (\text{C6})$$

Obviously, the equation $U_{21} = U_{43} = 0$ is established when satisfying

$$2k\pi\alpha - \alpha^2 - A_1^2 = 0. \quad (\text{C7})$$

As a result, the analytical solution of the pulse area A_1 is given by

$$A_1 = \pm \sqrt{\alpha(2k\pi - \alpha)}. \quad (\text{C8})$$

According to Eqs. (3a) and (3b), the pulse areas A_2 and A_3 can be rewritten as

$$A_2 = \pm A_1 \csc 2\theta_1 (\cos 2\theta_1 - \cos 2\theta_2), \quad (\text{C9a})$$

$$A_3 = \pm A_1 \csc 2\theta_1 \sin 2\theta_2. \quad (\text{C9b})$$

Through using Eqs. (C5) and (C8), we acquire the analytical expressions of A_2 and A_3 , i.e.,

$$A_2 = \pm 2(k\pi - \alpha), \quad (\text{C10a})$$

$$A_3 = \pm \sqrt{\alpha(2k\pi - \alpha)}. \quad (\text{C10b})$$

Finally, by substituting Eqs. (C5) and (C8) into Eq. (2), the expression for the propagator of this system in the basis $\{|1\rangle, |2\rangle, |3\rangle, |4\rangle\}$ reads

$$U = \begin{bmatrix} \cos \alpha & 0 & 0 & ie^{i\beta} \sin \alpha \\ 0 & \cos \alpha & ie^{i\varphi} \sin \alpha & 0 \\ 0 & ie^{-i\varphi} \sin \alpha & \cos \alpha & 0 \\ ie^{-i\beta} \sin \alpha & 0 & 0 & \cos \alpha \end{bmatrix}, \quad (\text{C11})$$

where

$$\beta = \phi + \varphi + \Phi. \quad (\text{C12})$$

Therefore, a universal single-qubit gate in the basis $\{|1\rangle, |4\rangle\}$,

$$U(\alpha, \beta) = \begin{bmatrix} \cos \alpha & ie^{i\beta} \sin \alpha \\ ie^{-i\beta} \sin \alpha & \cos \alpha \end{bmatrix}, \quad (\text{C13})$$

is achieved when the pulse areas and the phases satisfy

$$A_1 = A_3 = \pm \sqrt{\alpha(2k\pi - \alpha)}, \quad (\text{C14a})$$

$$A_2 = \pm 2(k\pi - \alpha), \quad (\text{C14b})$$

$$\beta = \phi + \varphi + \Phi, \quad (\text{C14c})$$

where k is a positive integer and $0 < \alpha < 2k\pi$.

For the second case (C3b), the derivation process is similar to the case (C3a). Substituting the parameters θ_1 and θ_2 into the equation $U_{21} = 0$ yields the expression for A_1 as follows:

$$A_1 = \pm \sqrt{-\alpha(2k\pi + \alpha)}, \quad (\text{C15})$$

where k is a negative integer and $-2k\pi < \alpha < 0$. It is easily seen that the form of the solution (C15) is the same as the previous one given by Eq. (C8) through setting $\alpha' = -\alpha$. Therefore, we only have to adopt the first solution (C14).

APPENDIX D: CORRELATED ERROR COMPENSATION BY COMPOSITE PULSES

In this Appendix, we first consider a case of three pulse areas with the same error, i.e., $\epsilon_1 = \epsilon_2 = \epsilon_3 = \epsilon$. For simplicity, the phases of CP sequences are assumed to be symmetric, i.e., $\Theta_n = \Theta_{N+1-n}$. In such a situation, the equations that the phases needs to satisfy become

$$P_{41}^N = |U_{41,\epsilon}^N|^2|_{\epsilon=0} = 1, \quad (\text{D1a})$$

$$s_k = \frac{\partial^k}{\partial \epsilon^k} |U_{41,\epsilon}^N|^2|_{\epsilon=0} = 0, \quad k = 1, 2, \dots \quad (\text{D1b})$$

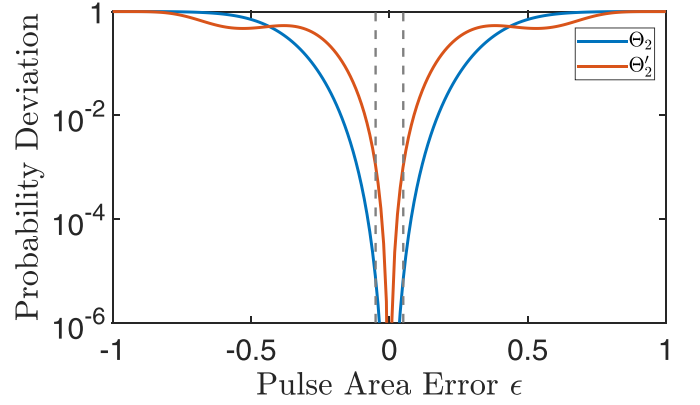


FIG. 7. Transition probability deviation $1 - P_{41,\epsilon}^3$ vs the pulse area error ϵ for different three-pulse sequences in a logarithmic scale, where the phases are given by Eq. (D4). The two gray lines indicate the pulse area errors in the interval $[-0.05, 0.05]$.

As an example, the total propagator of the three-pulse sequence reads

$$U_\epsilon^3 = U(\Theta_3)U(\Theta_2)U(\Theta_1), \quad (\text{D2})$$

with $\Theta_3 = \Theta_1$. In a similar manner, we set the first phases Θ_1 to zero, i.e., $\phi_1 = \varphi_1 = \Phi_1 = 0$. Again, the odd-order error coefficients in Eq. (D1b) automatically vanish, because they also contain the term $\sin k\pi$ or $\cos 3\alpha$. Therefore, we can use three controllable phases $\{\phi_2, \varphi_2, \Phi_2\}$ to solve the following equations:

$$s_2 = s_4 = s_6 = 0. \quad (\text{D3})$$

Unfortunately, it is verified that Eq. (D3) does not have solutions. There are two methods to address it. First, we can adopt cost functions [81,82] to find a set of optimal solutions for the phases. Such a method sacrifices a bit of accuracy while obtaining a broad range of error tolerance in exchange. Second, we can properly reduce the number of subequations. For example, we use these three phases to solve the first two subequations: $s_2 = s_4 = 0$. Here, we adopt the latter method, and there are two sets of solutions,

$$\Theta_2 = \{\phi_2, \varphi_2, \Phi_2\} = \left\{\frac{2}{3}, \frac{2}{3}, \frac{2}{3}\right\}\pi, \quad (\text{D4a})$$

$$\Theta'_2 = \{\phi_2, \varphi_2, \Phi_2\} = \left\{\frac{2}{3}, 1, \frac{2}{3}\right\}\pi. \quad (\text{D4b})$$

Note that both sets of solutions make the transition probability $P_{41,\epsilon}^3$ accurate to the sixth order in the pulse area error,

$$P_{41,\epsilon}^3 = 1 + O(\epsilon^6). \quad (\text{D5})$$

In Fig. 7, we plot the transition probability deviation $1 - P_{41,\epsilon}^3$ as a function of the pulse area error ϵ by using Eq. (D4). It

TABLE III. Phases (in units of π) of different five-pulse sequences for population inversion.

Index	ϕ_2	φ_2	Φ_2	ϕ_3	φ_3	Φ_3
$\Theta_{2,3}^1$	4/5	4/5	4/5	2/5	2/5	2/5
$\Theta_{2,3}^2$	0.498	0.751	0.493	1.362	1.792	1.352
$\Theta_{2,3}^3$	0.785	0.911	0.785	0.405	0.275	0.405

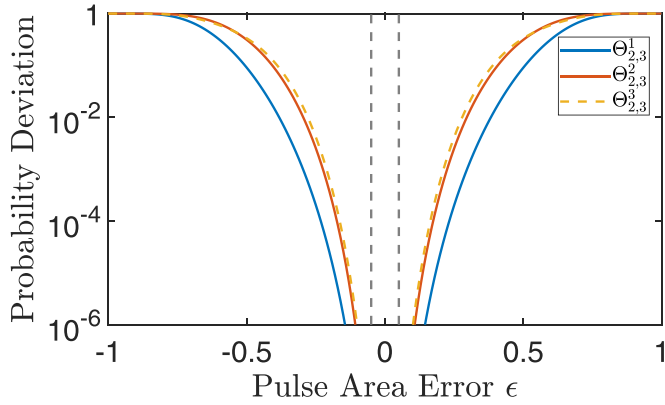


FIG. 8. Transition probability deviation $1 - P_{41,\epsilon}^5$ vs the pulse area error ϵ for different five-pulse sequences in a logarithmic scale, where $\Theta_{2,3}^n$ denotes the n th solution in Table III. The two gray lines indicate the pulse area errors in the interval $[-0.05, 0.05]$.

is easily found that the profile for Eq. (D4a) is wider than that of Eq. (D4b), because the sixth-order error coefficient of the former is much smaller than the latter. Considering some specific systems, such as NMR [9–12] and superconducting qubits [83,84], the ranges of errors are generally within 5%. Therefore, we plot in Fig. 7 two additional gray lines, which represent the pulse area errors in the interval $[-0.05, 0.05]$. When the pulse error rises to 5%, the three-pulse sequence using the phases in Eq. (D4b) fails to reach the threshold 10^{-4} [1]. Therefore, we prioritize Eq. (D4a) as the solution for the three-pulse sequence.

The total propagator of the five-pulse sequence reads

$$U_{\epsilon}^5 = U(\Theta_5)U(\Theta_4)U(\Theta_3)U(\Theta_2)U(\Theta_1), \quad (\text{D6})$$

with $\Theta_5 = \Theta_1$ and $\Theta_4 = \Theta_2$. We now have six controllable phases to solve the following equations:

$$s_2 = s_4 = s_6 = s_8 = 0. \quad (\text{D7})$$

These equations have many solutions, some of which are listed in Table III. The transition probability $P_{41,\epsilon}^5$ is accurate to the tenth order in the pulse area error,

$$P_{41,\epsilon}^5 = 1 + O(\epsilon^{10}). \quad (\text{D8})$$

Figure 8 shows the transition probability deviation $1 - P_{41,\epsilon}^5$ versus the pulse area error ϵ for different five-pulse sequences. It is obvious that the population deviation is much smaller than the threshold 10^{-4} for all five-pulse sequences when the pulse area error is 5%. Note that the profile for the first set of solutions is wider than that for the other two sets of solutions. Therefore, the phases for the five-pulse sequence are prioritized as $\Theta_{2,3}^1$. In Fig. 9(a), we plot the transition probability deviation for different pulse numbers, showing

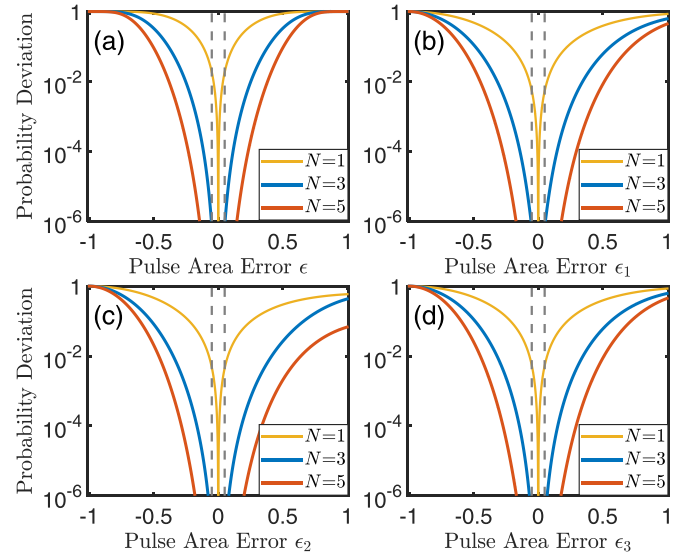


FIG. 9. Transition probability deviation $1 - P_{41,\epsilon}^N$ of the state $|4\rangle$ vs pulse area errors for different CP sequences with the pulse areas A_m satisfying Eq. (9). (a) $\epsilon_1 = \epsilon_2 = \epsilon_3 = \epsilon$. (b) $\epsilon_2 = \epsilon_3 = 0$. (c) $\epsilon_1 = \epsilon_3 = 0$. (d) $\epsilon_1 = \epsilon_2 = 0$. All phases are given in Table II.

that the robustness becomes stronger as the number of pulses increases.

Interestingly, the optimal solutions for Eqs. (D3) and (D7) are the same as in Ref. [85]. This implies that the four-level system may be regarded as a two-level one under some special assumptions (we assume the same pulse area errors and symmetric pulses here).

If only one of the pulse areas exhibits an error and the rest are accurate, we can still design specific CP sequences to compensate for it. In this case, the total propagators of the three- and five-pulse sequences become

$$U_{\epsilon_m}^3 = U(\Theta_3)U(\Theta_2)U(\Theta_1), \quad (\text{D9})$$

$$U_{\epsilon_m}^5 = U(\Theta_5)U(\Theta_4)U(\Theta_3)U(\Theta_2)U(\Theta_1), \quad (\text{D10})$$

where the corresponding solutions are listed in Table II. Figures 9(b)–9(d) show the transition probability deviation $1 - P_{41,\epsilon}^N$ of the state $|4\rangle$ as a function of the pulse area errors ϵ_m for different pulse numbers. Obviously, the CP sequences also have strong robustness against a single type of pulse area errors. The comparison of Figs. 9(b)–9(d) to Fig. 9(a) indicates that under the same number of pulses, the profiles for the $U_{\epsilon_m}^N$ sequences are superior to that for the U_{ϵ}^N sequences. It is responsible for the fact that one can nullify more error coefficients in the single error case. We also notice that the profiles for the $U_{\epsilon_1}^N$ and $U_{\epsilon_3}^N$ sequences are identical, resulting from the symmetric pulse areas in the propagator (2).

- [1] M. A. Nielsen and I. L. Chuang, *Quantum Computation and Quantum Information* (Cambridge University Press, Cambridge, 2000).
 [2] N. V. Vitanov, T. Halfmann, B. W. Shore, and K. Bergmann, Laser-induced population transfer by adiabatic passage techniques, *Annu. Rev. Phys. Chem.* **52**, 763 (2001).

- [3] D. Guéry-Odelin, A. Ruschhaupt, A. Kiely, E. Torrontegui, S. Martínez-Garaot, and J. G. Muga, Shortcuts to adiabaticity: Concepts, methods, and applications, *Rev. Mod. Phys.* **91**, 045001 (2019).
 [4] F. Motzoi, J. M. Gambetta, P. Rebentrost, and F. K. Wilhelm, Simple pulses for elimination of leakage in

- weakly nonlinear qubits, *Phys. Rev. Lett.* **103**, 110501 (2009).
- [5] D. Daems, A. Ruschhaupt, D. Sugny, and S. Guérin, Robust quantum control by a single-shot shaped pulse, *Phys. Rev. Lett.* **111**, 050404 (2013).
- [6] J. Zhang, Y.-X. Liu, R.-B. Wu, K. Jacobs, and F. Nori, Quantum feedback: Theory, experiments, and applications, *Phys. Rep.* **679**, 1 (2017).
- [7] P. Král, I. Thanopoulos, and M. Shapiro, Colloquium: Coherently controlled adiabatic passage, *Rev. Mod. Phys.* **79**, 53 (2007).
- [8] N. V. Vitanov, A. A. Rangelov, B. W. Shore, and K. Bergmann, Stimulated Raman adiabatic passage in physics, chemistry, and beyond, *Rev. Mod. Phys.* **89**, 015006 (2017).
- [9] M. H. Levitt and R. Freeman, NMR population inversion using a composite pulse, *J. Magn. Reson.* **33**, 473 (1979).
- [10] M. H. Levitt, Composite pulses, *Prog. Nucl. Magn. Res. Spectrosc.* **18**, 61 (1986).
- [11] S. Wimperis, Iterative schemes for phase-distortionless composite 180° pulses, *J. Magn. Res.* **93**, 199 (1991).
- [12] S. Wimperis, Broadband, narrowband, and passband composite pulses for use in advanced NMR experiments, *J. Magn. Reson., Ser. A* **109**, 221 (1994).
- [13] S. Husain, M. Kawamura, and J. A. Jones, Further analysis of some symmetric and antisymmetric composite pulses for tackling pulse strength errors, *J. Magn. Reson.* **230**, 145 (2013).
- [14] J. A. Jones, Quantum computing with NMR, *Prog. Nucl. Magn. Res. Spectrosc.* **59**, 91 (2011).
- [15] S. Gulde, M. Riebe, G. P. T. Lancaster, C. Becher, H. Eschner, H. Haffner, F. Schmidt-Kaler, I. Chuang, and R. Blatt, Implementation of the Deutsch-Josza algorithm on an ion trap quantum computer, *Nature (London)* **421**, 48 (2003).
- [16] F. Schmidt-Kaler, H. Haffner, M. Riebe, S. Gulde, G. Lancaster, T. Deuschle, C. Becher, C. F. Roos, J. Eschner, and R. Blatt, Realization of the Cirac-Zoller controlled-NOT quantum gate, *Nature (London)* **422**, 408 (2003).
- [17] H. Haffner, C. F. Roos, and R. Blatt, Quantum computing with trapped ions, *Phys. Rep.* **469**, 155 (2008).
- [18] N. Timoney, V. Elman, S. Glaser, C. Weiss, M. Johanning, W. Neuhauser, and C. Wunderlich, Error-resistant single-qubit gates with trapped ions, *Phys. Rev. A* **77**, 052334 (2008).
- [19] T. Monz, K. Kim, W. Hänsel, M. Riebe, A. S. Villar, P. Schindler, M. Chwalla, M. Hennrich, and R. Blatt, Realization of the quantum Toffoli gate with trapped ions, *Phys. Rev. Lett.* **102**, 040501 (2009).
- [20] C. M. Shappert, J. T. Merrill, K. R. Brown, J. M. Amini, C. Volin, S. C. Doret, H. Hayden, C.-S. Pai, K. R. Brown, and A. W. Harter, Spatially uniform single-qubit gate operations with near-field microwaves and composite pulse compensation, *New J. Phys.* **15**, 083053 (2013).
- [21] E. Mount, C. Kabytayev, S. Crain, R. Harper, S. Y. Baek, G. Vrijsen, S. T. Flammia, K. R. Brown, P. Maunz, and J. Kim, Error compensation of single-qubit gates in a surface-electrode ion trap using composite pulses, *Phys. Rev. A* **92**, 060301(R) (2015).
- [22] N. V. Vitanov, T. F. Gloger, P. Kaufmann, D. Kaufmann, T. Collath, M. Tanveer Baig, M. Johanning, and C. Wunderlich, Fault-tolerant Hahn-Ramsey interferometry with pulse sequences of alternating detuning, *Phys. Rev. A* **91**, 033406 (2015).
- [23] J. Randall, A. M. Lawrence, S. C. Webster, S. Weidt, N. V. Vitanov, and W. K. Hensinger, Generation of high-fidelity quantum control methods for multilevel systems, *Phys. Rev. A* **98**, 043414 (2018).
- [24] T. Sriarunothai, S. Wlk, G. S. Giri, N. Friis, V. Dunjko, H. J. Briegel, and C. Wunderlich, Speeding-up the decision making of a learning agent using an ion trap quantum processor, *Quantum Sci. Technol.* **4**, 015014 (2018).
- [25] D. L. Butts, K. Kotru, J. M. Kinast, A. M. Radojevic, B. P. Timmons, and R. E. Stoner, Efficient broadband Raman pulses for large-area atom interferometry, *J. Opt. Soc. Am. B* **30**, 922 (2013).
- [26] A. Dunning, R. Gregory, J. Bateman, N. Cooper, M. Himsworth, J. A. Jones, and T. Freegarde, Composite pulses for interferometry in a thermal cold atom cloud, *Phys. Rev. A* **90**, 033608 (2014).
- [27] P. Berg, S. Abend, G. Tackmann, C. Schubert, E. Giese, W. P. Schleich, F. A. Narducci, W. Ertmer, and E. M. Rasel, Composite-light-pulse technique for high-precision atom interferometry, *Phys. Rev. Lett.* **114**, 063002 (2015).
- [28] J. P. Kestner, X. Wang, L. S. Bishop, E. Barnes, and S. Das Sarma, Noise-resistant control for a spin qubit array, *Phys. Rev. Lett.* **110**, 140502 (2013).
- [29] C. X. Zhang, R. E. Throckmorton, X. C. Yang, X. Wang, E. Barnes, and S. Das Sarma, Randomized benchmarking of barrier versus tilt control of a singlet-triplet qubit, *Phys. Rev. Lett.* **118**, 216802 (2017).
- [30] G. T. Hickman, X. Wang, J. P. Kestner, and S. Das Sarma, Dynamically corrected gates for an exchange-only qubit, *Phys. Rev. B* **88**, 161303(R) (2013).
- [31] B. T. Torosov and N. V. Vitanov, High-fidelity composite quantum gates for Raman qubits, *Phys. Rev. Res.* **2**, 043194 (2020).
- [32] Z. C. Shi, H. N. Wu, L. T. Shen, J. Song, Y. Xia, X. X. Yi, and S. B. Zheng, Robust single-qubit gates by composite pulses in three-level systems, *Phys. Rev. A* **103**, 052612 (2021).
- [33] H. L. Gevorgyan and N. V. Vitanov, Ultrahigh-fidelity composite rotational quantum gates, *Phys. Rev. A* **104**, 012609 (2021).
- [34] B. T. Torosov, M. Drewsen, and N. V. Vitanov, Efficient and robust chiral resolution by composite pulses, *Phys. Rev. A* **101**, 063401 (2020).
- [35] B. T. Torosov, M. Drewsen, and N. V. Vitanov, Chiral resolution by composite Raman pulses, *Phys. Rev. Res.* **2**, 043235 (2020).
- [36] G. T. Genov, D. Schraft, T. Halfmann, and N. V. Vitanov, Correction of arbitrary field errors in population inversion of quantum systems by universal composite pulses, *Phys. Rev. Lett.* **113**, 043001 (2014).
- [37] B. T. Torosov and N. V. Vitanov, Arbitrarily accurate twin composite π -pulse sequences, *Phys. Rev. A* **97**, 043408 (2018).
- [38] C. Zhang, Y. Liu, Z. C. Shi, J. Song, Y. Xia, and S. B. Zheng, Robust population inversion in three-level systems by composite pulses, *Phys. Rev. A* **105**, 042414 (2022).
- [39] S. S. Ivanov, B. T. Torosov, and N. V. Vitanov, High-fidelity quantum control by polychromatic pulse trains, *Phys. Rev. Lett.* **129**, 240505 (2022).
- [40] B. T. Torosov and N. V. Vitanov, Experimental demonstration of composite pulses on IBM's quantum computer, *Phys. Rev. Appl.* **18**, 034062 (2022).

- [41] M. Ringbauer, M. Meth, L. Postler, R. S. R. Blatt, P. Schindler, and T. Monz, A universal qudit quantum processor with trapped ions, *Nat. Phys.* **18**, 1053 (2022).
- [42] P. Schindler, D. Nigg, T. Monz, J. T. Barreiro, E. Martinez, S. X. Wang, S. Quint, M. F. Brandl, V. Nebendahl, C. F. Roos, M. Chwalla, M. Hennrich, and R. Blatt, A quantum information processor with trapped ions, *New J. Phys.* **15**, 123012 (2013).
- [43] K. J. Satzinger, Y.-J. Liu, A. Smith, C. Knapp, M. Newman, C. Jones, Z. Chen, C. Quintana, X. Mi, A. Dunsworth *et al.*, Realizing topologically ordered states on a quantum processor computer, *Science* **374**, 1237 (2021).
- [44] P. J. J. O'Malley, R. Babbush, I. D. Kivlichan, J. Romero, J. R. McClean, R. Barends, J. Kelly, P. Roushan, A. Tranter, N. Ding, B. Campbell, Y. Chen, Z. Chen, B. Chiaro, A. Dunsworth, A. G. Fowler, E. Jeffrey, E. Lucero, A. Megrant, J. Y. Mutus *et al.*, Scalable quantum simulation of molecular energies, *Phys. Rev. X* **6**, 031007 (2016).
- [45] W. J. Huggins, B. A. O'Gorman, D. R. Rubin, N. C. Reichman, and J. Lee, Unbiasing fermionic quantum monte carlo with a quantum computer, *Nature (London)* **603**, 416 (2022).
- [46] D. Gottesman, Fault-tolerant quantum computation with higher-dimensional systems, *Chaos Solitons Fractals* **10**, 1749 (1999).
- [47] Y. Wang, Z. Hu, B. C. Sanders, and S. Kais, Qudits and high-dimensional quantum computing, *Front. Phys.* **8**, 589504 (2022).
- [48] P. Liu, R. Wang, J.-N. Zhang, Y. Zhang, X. Cai, H. Xu, Z. Li, J. Han, X. Li, G. Xue, W. Liu, L. You, Y. Jin, and H. Yu, Performing $SU(d)$ operations and rudimentary algorithms in a superconducting transmon qudit for $d = 3$ and $d = 4$, *Phys. Rev. X* **13**, 021028 (2023).
- [49] Y. L. Chi, J. S. Huang, Z. C. Zhang, J. Mao, Z. N. Zhou, X. J. Chen, C. H. Zhai, J. M. Bao, T. X. Dai, H. H. Yuan, M. Zhang, D. X. Dai, B. Tang, Y. Yang, Z. H. Li, Y. H. Ding, O. L. K., M. G. Thompson, J. L. O'Brien, Y. Li *et al.*, A programmable qudit-based quantum processor, *Nat. Commun.* **13**, 1166 (2022).
- [50] J. Qian, J. J. Zhai, L. Zhang, and W. P. Zhang, Chirped multi-photon adiabatic passage for a four-level ladder-type Rydberg excitation, *Phys. Rev. A* **91**, 013411 (2015).
- [51] H. C. Li, G. Q. Ge, and M. S. Zubairy, Achieving nonlinear optical modulation via four-wave mixing in a four-level atomic system, *Phys. Rev. A* **97**, 053826 (2018).
- [52] P. G. Zhong, C. Li, Y. Wang, J. Song, S. T. Liu, Y. Y. Jiang, and Y. Xia, Quantum phase transitions triggered by a four-level atomic system in dissipative environments, *Phys. Rev. A* **99**, 043829 (2019).
- [53] J. L. Rubio, J. Mompert, and V. Ahufinger, Quantum-jump analysis of frequency up-conversion amplification without inversion in a four-level scheme, *Phys. Rev. A* **107**, 013707 (2023).
- [54] C. Meng, T. Shui, and W. X. Yang, Coherent transfer of optical vortices via backward four-wave mixing in a double- Λ atomic system, *Phys. Rev. A* **107**, 053712 (2023).
- [55] Y. C. Li, D. Martínez-Cercós, S. Martínez-Garaot, X. Chen, and J. G. Muga, Hamiltonian design to prepare arbitrary states of four-level systems, *Phys. Rev. A* **97**, 013830 (2018).
- [56] Y. H. Kang, Y. H. Chen, Z. C. Shi, B. H. Huang, J. Song, and Y. Xia, Pulse design for multilevel systems by utilizing Lie transforms, *Phys. Rev. A* **97**, 033407 (2018).
- [57] P. J. Low, B. M. White, A. A. Cox, M. L. Day, and C. Senko, Practical trapped-ion protocols for universal qudit-based quantum computing, *Phys. Rev. Res.* **2**, 033128 (2020).
- [58] P. Kumar and S. Dasgupta, Optical switching and bistability in four-level atomic systems, *Phys. Rev. A* **94**, 023851 (2016).
- [59] W. H. Xu and J. Y. Gao, Absorption mechanism in a four-level system, *Phys. Rev. A* **67**, 033816 (2003).
- [60] S. Rebić, D. Vitali, C. Ottaviani, P. Tombesi, M. Artoni, F. Cataliotti, and R. Corbalán, Polarization phase gate with a tripod atomic system, *Phys. Rev. A* **70**, 032317 (2004).
- [61] B. Q. Ou, L. M. Liang, and C. Z. Li, Quantum coherence effects in a four-level diamond-shape atomic system, *Opt. Commun.* **282**, 2870 (2009).
- [62] M. Christandl, N. Datta, A. Ekert, and A. J. Landahl, Perfect state transfer in quantum spin networks, *Phys. Rev. Lett.* **92**, 187902 (2004).
- [63] B. H. Huang, Y. H. Kang, Y. H. Chen, Z. C. Shi, J. Song, and Y. Xia, Quantum state transfer in spin chains via shortcuts to adiabaticity, *Phys. Rev. A* **97**, 012333 (2018).
- [64] Y. Xue, G. Wang, J.-H. Wu, and J.-Y. Gao, Optical gain properties in a coherently prepared four-level cold atomic system, *Phys. Rev. A* **75**, 063832 (2007).
- [65] T. Y. Abi-Salloum, B. Henry, J. P. Davis, and F. A. Narducci, Resonances and excitation pathways in four-level N-scheme atomic systems, *Phys. Rev. A* **82**, 013834 (2010).
- [66] S. E. Harris and Y. Yamamoto, Photon switching by quantum interference, *Phys. Rev. Lett.* **81**, 3611 (1998).
- [67] H. Kang, G. Hernandez, and Y. Zhu, Superluminal and slow light propagation in cold atoms, *Phys. Rev. A* **70**, 011801(R) (2004).
- [68] A. Alexandrescu, J. R. Salgueiro, V. M. Pérez-García, and H. Michinel, Nonperturbative vector solitary waves in four-level coherent media, *Phys. Rev. A* **79**, 063843 (2009).
- [69] G. F. Sinclair and N. Korolkova, Effective cross-Kerr Hamiltonian for a nonresonant four-level atom, *Phys. Rev. A* **77**, 033843 (2008).
- [70] G. F. Sinclair and N. Korolkova, Cross-Kerr interaction in a four-level atomic system, *Phys. Rev. A* **76**, 033803 (2007).
- [71] C. Goren, A. D. Wilson-Gordon, M. Rosenbluh, and H. Friedmann, Atomic four-level N systems, *Phys. Rev. A* **69**, 053818 (2004).
- [72] T. Haase, G. Alber, and V. M. Stojanović, Conversion from W to Greenberger-Horne-Zeilinger states in the Rydberg-blockade regime of neutral-atom systems: Dynamical-symmetry-based approach, *Phys. Rev. A* **103**, 032427 (2021).
- [73] R. H. Zheng, Y. H. Kang, D. Ran, Z. C. Shi, and Y. Xia, Deterministic interconversions between the Greenberger-Horne-Zeilinger states and the W states by invariant-based pulse design, *Phys. Rev. A* **101**, 012345 (2020).
- [74] J. K. Nauth and V. M. Stojanović, Quantum-brachistochrone approach to the conversion from W to Greenberger-Horne-Zeilinger states for Rydberg-atom qubits, *Phys. Rev. A* **106**, 032605 (2022).
- [75] G. Y. Wang, D. Y. Wang, W. X. Cui, H. F. Wang, A. D. Zhu, and S. Zhang, Direct conversion of a three-atom W state to a Greenberger-Horne-Zeilinger state in spatially separated cavities, *J. Phys. B* **49**, 065501 (2016).
- [76] J. Song, X. D. Sun, Q. X. Mu, L. L. Zhang, Y. Xia, and H. S. Song, Direct conversion of a four-atom W state to a

- Greenberger-Horne-Zeilinger state via a dissipative process, *Phys. Rev. A* **88**, 024305 (2013).
- [77] P. Walther, K. J. Resch, and A. Zeilinger, Local conversion of Greenberger-Horne-Zeilinger states to approximate W states, *Phys. Rev. Lett.* **94**, 240501 (2005).
- [78] W. X. Cui, S. Hu, H. F. Wang, A. D. Zhu, and S. Zhang, Deterministic conversion of a four-photon GHZ state to a W state via homodyne measurement, *Opt. Express* **24**, 15319 (2016).
- [79] Y. H. Kang, Z. C. Shi, B. H. Huang, J. Song, and Y. Xia, Deterministic conversions between Greenberger-Horne-Zeilinger states and W states of spin qubits via Lie-transform-based inverse Hamiltonian engineering, *Phys. Rev. A* **100**, 012332 (2019).
- [80] Y. Nagai, Y. Ota, and K. Tanaka, Time-reversal symmetry breaking and gapped surface states due to spontaneous emergence of new order in d -wave nanoislands, *Phys. Rev. B* **96**, 060503(R) (2017).
- [81] Z. C. Shi, C. Zhang, D. Ran, Y. Xia, R. Ianculescu, A. Friedman, X. X. Yi, and S. B. Zheng, Composite pulses for high fidelity population transfer in three-level systems, *New J. Phys.* **24**, 023014 (2022).
- [82] H. N. Wu, C. Zhang, J. Song, Y. Xia, and Z. C. Shi, Composite pulses for optimal robust control in two-level systems, *Phys. Rev. A* **107**, 023103 (2023).
- [83] K. W. Murch, U. Vool, D. Zhou, S. J. Weber, S. M. Girvin, and I. Siddiqi, Cavity-assisted quantum bath engineering, *Phys. Rev. Lett.* **109**, 183602 (2012).
- [84] R. H. Zheng, W. Ning, Z. B. Yang, Y. Xia, and S. B. Zheng, Demonstration of dynamical control of three-level open systems with a superconducting qutrit, *New J. Phys.* **24**, 063031 (2022).
- [85] B. T. Torosov and N. V. Vitanov, Smooth composite pulses for high-fidelity quantum information processing, *Phys. Rev. A* **83**, 053420 (2011).